Research Article

Understanding oxidation resistance of Pt-based alloys through computations of Ellingham diagrams with experimental verifications

Xiaoyu Chong[1], Wei Yu[1], Yingxue Liang[1], Shun-Li Shang[2,*], Chao Li[1], Aimin Zhang[3], Yan Wei[3], Xingyu Gao[4], Yi Wang[2], Jing Feng[1,*], Li Chen[3], Haifeng Song[4], Zi-Kui Liu[2]

[1]Faculty of Materials Science and Engineering, Kunming University of Science and Technology, Kunming 650093, Yunnan, China.
[2]Department of Materials Science and Engineering, The Pennsylvania State University, University Park, PA 16802, USA.
[3]Yunnan Precious Metal Laboratory Co. LTD, Kunming 650106, Yunnan, China.
[4]Laboratory of Computational Physics, Institute of Applied Physics and Computational Mathematics, Beijing 100088, China.

***Correspondence to:** Prof. Shun-Li Shang, Department of Materials Science and Engineering, The Pennsylvania State University, 324 Steidle Building, University Park, PA 16802, USA. E-mail: sus26@psu.edu.cn; Prof. Jing Feng, Faculty of Materials Science and Engineering, Kunming University of Science and Technology, 326 Materials Science and Engineering Building, Xuefu Road, Kunming 650093, Yunnan, China. E-mail: jingfeng@kust.edu.cn

How to cite this article: Chong X, Yu W, Liang Y, Shang SL, Li C, Zhang A, Wei Y, Gao X, Wang Y, Feng J, Chen L, Song H, Liu ZK. Understanding oxidation resistance of Pt-based alloys through computations of Ellingham diagrams with experimental verifications. *J Mater Inf* 2023;3:21. https://dx.doi.org/10.20517/jmi.2023.17

Abstract

Thermodynamic calculations of Ellingham diagrams and the forming oxides have been performed relevant to the Pt-based alloys $Pt_{82}Al_{12}M_6$ (M = Cr, Hf, Pt, and Ta). The predicted Ellingham diagrams indicate that the elements Hf and Al are easy to oxidize, followed by Ta and Cr, while Pt is extremely difficult to oxidize. Oxidation experiments characterized by X-ray diffraction (XRD) and electron probe micro-analyzers verify the present thermodynamic predictions, showing that the best alloy with superior oxidation resistance is $Pt_{82}Al_{12}Cr_6$, followed by $Pt_{88}Al_{12}$ due to the formation of the dense and continuous α-Al_2O_3 scale on the surface of alloys; while the worse alloy is $Pt_{82}Al_{12}Hf_6$ followed by $Pt_{82}Al_{12}Ta_6$ due to drastic internal oxidation and the formation of deleterious HfO_2, $AlTaO_4$, and Ta_2O_5. The present work, combining computations with experimental verifications, provides a fundamental understanding and knowledgebase to develop Pt-based superalloys with superior oxidation resistance that can be used in ultra-high temperatures.

Keywords: Ellingham diagrams, Pt-based alloys, oxidation resistance, XRD, EPMA

INTRODUCTION

Aiming to design ultra-high-temperature materials for use in harsh environments has led to the development of Pt-based superalloys. These superalloys are superior to Ni-based superalloys since Pt has a higher melting point (2,042 K for Pt *vs.* 1,728 K for Ni[1]) and is more chemically inert for outstanding oxidation resistance, c.f., the predicted Ellingham diagrams[2] in the present work. Currently, a higher application temperature is urgently needed in gas turbine sections to improve engine efficiency and reduce fuel consumption and carbon dioxide emissions for a greater thrust. For example, the current application temperature of Pt-based superalloys can be extended to 1,350 °C (1,623 K)[3]. Although Pt-based alloys are expensive, they are the most reliable materials under ultrahigh temperatures and are widely used as bonding coating alloys in the thermal barrier coating (TBC) system and in the aerospace engine nozzle. The excellent oxidation resistance of Pt-based superalloys is their great advantage. The oxidation behavior of pure Pt has been fully investigated[4]; however, the oxidation of Pt-Al-based alloys is far from fully understood.

The Pt-Al system is one of the widely used superalloys, fueling up considerable studies such as the strength and creep properties[5,6]. The mechanism of oxidation resistance for pure Pt and Pt-Al alloys is quite different. It shows that the Pt-Al alloy can be further stabilized at high temperatures in terms of the $L1_2$-based γ' phase by adding alloying elements such as Cr, Hf, and Ta. Especially, Cr can form the dense and continue Cr_2O_3 coating to provide a protective scale on Cr-containing alloys; Hf is a reactive element to reduce the growth of a thermally grown Al_2O_3 scale in alloys such as the NiAlCr and NiAlPt[7]; additionally, Ta can hinder ion diffusion and improve oxidation resistance in, e.g., the Ni-10Al alloy[8]. One of the purposes of the present work is to develop a series of Pt-Al-based alloys with strong oxidation resistance used as bonding coating in the TBC system. Notably, oxidation resistance for an alloy of interest is an important indicator to determine whether it can be applied to high temperatures or not[9,10], with the best oxide being α-Al_2O_3 (represented by Al_2O_3 in the present work if no further explanation), which will be formed on the surface of Al-containing alloys at high temperatures (> 1,100 °C)[11-13]. Here, Al_2O_3 usually acts as the oxidation resistance barrier of the alloys at high temperatures, thus further preventing oxidation inside the alloys[14,15].

In the present work, four alloying elements, Al, Cr, Hf, and Ta, are selected to investigate oxidation resistance of the Pt-based alloys. The forming mechanism of Al_2O_3 and other oxides is understood by the predicted Ellingham diagrams[2] with experimental verifications. Here, the free energy (or partial pressure of gas species) versus temperature diagram, i.e., the Ellingham diagram, is a predictive tool to tailor thermodynamic stability of oxides that form in the present Pt-based alloys[16]. In addition, the oxidation kinetic curves are also measured to examine the formation rates of oxides. The present computations of Ellingham diagrams with experimental verifications provide fundamentals to develop Pt-based superalloys with superior oxidation resistance that can be used in ultra-high temperatures.

MATERIALS AND METHODS
Ellingham diagram
An Ellingham diagram[2] is a plot regarding the change of the standard Gibbs energy (ΔG^o) as a function of temperature for a given reaction, evaluating the equilibrium phases obtained by chemical reactions. In the present work, the calculated Ellingham diagrams can judge whether the Pt-based alloys (i.e., metals M = Al, Cr, Hf, Pt, and/or Ta) can be oxidized or not in terms of the following two reactions (scenarios),

$$\frac{2x}{y}M(s \ or \ l) + O_2(g) = \frac{2}{y}M_xO_y(s \ or \ l) \tag{1}$$

$$\frac{2x}{ay-bx}M_aO_b(s \ or \ l) + O_2(g) = \frac{2a}{ay-bx}M_xO_y(s \ or \ l) \tag{2}$$

where *s*, *l*, and *g* indicate the solid, liquid, and gas phases, respectively. Here, (i) $ay > bx$, indicating the oxidation is from M_aO_b to M_xO_y; (ii) the oxygen gas species O_2 is selected due to its extreme dominance in comparison with the other oxygen species of O_1 and O_3[17]; and (iii) the reactions are under the total pressure of 1 atm with 1 mole of O_2. Under the assumptions of (a) ideal gas with O_2 being the dominant gas species and (b) the activities of liquids and solids as unity, the ΔG^o of equation (1) or (2) at equilibrium can be determined by the activity of oxygen (a_{O_2})[18], as described by the equation:

$$\Delta G^o = RT \ln a_{O_2} \tag{3}$$

where R is the gas constant, and T is the absolute temperature. By setting the reference pressure and the total pressure $P_{ref} = P_{tot} = 1$ atm (10^5 Pa), then, $a_{O_2} = P_{O_2}/P_{ref}$ with P_{O_2} being the partial pressure of O_2. Note that (a) only the stable or metastable oxides at 1 atm are considered in the present work; and (b) the reactions in equations (1) and (2) only involve the phases that are able to be in equilibrium with each other, i.e., only the phases involving neighboring oxidation states are allowed in a reaction. For example, the oxidation in the Cr-O system is from Cr to Cr_2O_3 and then to Cr_5O_{12} with increasing oxygen content, x(O). For the ternary oxide of $AlTaO_4$ with x(O) = 0.667, only the reaction from the oxide with x(O) = 0.6 (i.e., Al_2O_3) is considered. Table 1 summarizes all the possible reactions to form oxides in the present Al-Cr-Hf-Pt-Ta-O system, including seven binary oxides (Al_2O_3, Cr_2O_3, Cr_5O_{12}, HfO_2, PtO, PtO_2, and Ta_2O_5) and 1 ternary oxide ($AlTaO_4$). Note that the listed reaction to form NiO is for reference only, and four polymorphs of Al_2O_3 (α-Al_2O_3, δ-Al_2O_3, γ-Al_2O_3, and κ-Al_2O_3) were included in the SGTE substance database (i.e., the SSUB5)[19] but only α-Al_2O_3 is stable.

Thermodynamic database and thermodynamic calculations

Calculating Ellingham diagrams requires a thermodynamic database (TDB) for the present Al-Cr-Hf-Pt-Ta-O system, which was created by a combination of the metal system Al-Cr-Hf-Pt modeled by Kim[20] with a thermodynamic description of the binary oxides from the SSUB5 database[19]. The missing thermodynamic properties of the Pt-O compounds (PtO, PtO_2, and Pt_3O_4) were added to SSUB5 using the reported enthalpies and entropies of formation at room temperature[4]. The missing thermodynamic properties of $AlTaO_4$ were estimated with the reference states being the binary oxides in SSUB5,

$$Al_2O_3 + Ta_2O_5 = AlTaO_4 \tag{4}$$

The enthalpy of formation (ΔH) of equation (4) was predicted by the density functional theory (DFT)-based first-principles calculations using the Vienna *Ab initio* Simulation Package (VASP)[21]. The ion-electron interaction was described by the projector augmented wave (PAW) method[22], and the exchange-correlation (X-C) functionals were described by the local density approximation (LDA)[23] and the generalized gradient approximation (GGA) improved for densely packed solids and their surfaces (PBEsol)[24]. Other details of first-principles calculations are given in Table 2, as well as the default settings used by the software DFT Tool Kits (DFTTK)[25], including crystal structures of the three oxides, the used *k*-point meshes, the employed plane-wave cutoff energy, and the selected potentials for elements Al, Ta, and O. In addition, Table 2 also lists the DFT results reported by the Materials Project (MP)[26] and

Table 1. Reactions of one mole of O_2 (g) from metal and/or metal oxide to metal oxide. The mole fractions of oxygen content, x(O), in oxides, and the P_{O_2} value (in Torr) for each reaction at 1,300 °C and 1 atm are also shown. The reaction numbers (No.) are given according to the descending order of these P_{O_2} values, and the reaction No. 4 to form NiO is for reference only

No.	Metals	x(O)	P_{O_2} at 1,300 °C	Reactions
1	Pt	0.50 to 0.67	1.279e + 08	$2PtO + O_2 = 2PtO_2$
2	Cr	0.60 to 0.71	1.151e + 08	$\frac{10}{9}Cr_2O_3 + O_2 = \frac{4}{9}Cr_5O_{12}$
3	Pt	0.50	2.036e + 07	$2Pt + O_2 = 2PtO$
4	Ni	0.50	1.306e - 04	$2Ni + O_2 = 2NiO$
5	Cr	0.60	4.660e - 14	$\frac{4}{3}Cr + O_2 = \frac{2}{3}Cr_2O_3$
6	Ta	0.71	4.426e - 16	$\frac{4}{5}Ta + O_2 = \frac{2}{5}Ta_2O_5$
7	Al, Ta	0.60 to 0.67	1.939e - 16	$\frac{2}{5}Al_2O_3 + \frac{4}{5}Ta + O_2 = \frac{4}{5}AlTaO_4$
8	Al	0.60	8.256e - 24	$\frac{4}{3}Al + O_2 = \frac{2}{3}Al_2O_3$
9	Hf	0.67	1.553e - 25	$Hf + O_2 = HfO_2$

Table 2. Enthalpy of formation (H) for the reaction of "$Al_2O_3 + Ta_2O_5 = AlTaO_4$" based on DFT-based first-principles calculations at 0 K according to MP[26], OQMD[27], and the present work, where the IDs of MP and OQMD are also listed. The final cutoff energy for accurate energy is 520 eV, and the other details are the default ones adopted by DFTTK[25]

Oxides	Space group	ID and notes	X-C functionals	Total energy (eV/atom)	H (J/6-mole-atoms)
Al_2O_3 $(4 \times 4 \times 4)$[a]	$R\bar{3}c$	MP-1143	PBE	-7.48	
		OQMD-1234774	PBE	-7.477	
		This work	PBEsol	-7.388	
		This work	LDA	-8.313	
Ta_2O_5 $(6 \times 5 \times 1)$[b]	$Pmmn$	MP-1539317	PBE	-9.77	
		OQMD-1739439	PBE	-9.759	
		This work	PBEsol	-9.621	
		This work	LDA	-10.605	
$AlTaO_4$ $(4 \times 4 \times 5)$[c]	C12/m1	MP-14333	PBE	-8.84	-13990
		OQMD-6370	PBE	-8.837	-16692
		This work	PBEsol	-8.714	-13490[d]
		This work	LDA	-9.669	-11091

[a]*k*-point mesh used for the 10-atom cell; [b]*k*-point mesh used for the 14-atom cell; [c]*k*-point mesh used for the 12-atom cell; [d]This value was adopted in the TDB. DFTTK: DFT Tool Kits; IDs: Identification numbers; LDA: local density approximation; MP: materials project; OQMD: Open Quantum Materials Database; TDB: thermodynamic database; VASP: Vienna *Ab initio* Simulation Package.

the Open Quantum Materials Database (OQMD)[27] using the X-C functional of GGA-PBE[28]. It shows that the (ΔH) value by PBEsol (-13490 J per 6-mole-atoms) is roughly in the middle of these (ΔH) values and hence was selected for equation (4) and implemented into SSUB5 together with the heat capacity of AlTaO$_4$ estimated by the Neumann-Kopp rule[29,30].

In the present work, thermodynamic calculations were performed by using the Thermo-Calc software[31] and the presently built TDB (i.e., the TDB file, as shown in the Supplementary Material). Rather than calculating ΔG° directly for each reaction in Table 1, equilibrium calculations were performed in the present work using the following conditions for each reaction: (i) the total pressure fixed at 1 atm; (ii) 1 mole of O$_2$; and (iii) the dormant gas and other phases, which were excluded in the reactions of interest; see more details and a macro tcm file in our recent work[18].
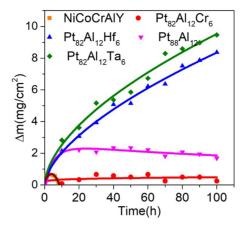
Figure 1. The oxidation kinetics of four Pt-based alloys and NiCoCrAlY after oxidation at 1,300 °C for 100 h in an air atmosphere.

Experiments

The ingots were prepared by arc-melting. Then, the ingots were subjected to vacuum heat treatments. It was determined that the alloys include the $L1_2$-type γ'-Pt_3Al phase. The square samples with the dimensions of 3 mm (length) × 3 mm (width) × 1 mm (thickness) were extracted from the as-cast ingots. All the samples were ground with the SiC abrasive papers (3,000 mesh) and then polished in 1 μm diamond suspension, and cleaned repeatedly in the ethanol solution. The oxidation experiments were carried out in the air at 1,300 °C using the high-temperature tube furnace. The samples were taken out after different oxidation times (1 to 100 h) at 1,300 °C and cooled down to room temperature within 15 min. After weighing by an electronic balance, the sample and crucible were preheated and put into the furnace. The sample was heated up to 1,300 °C within 3 min. An X-ray diffractometer was used to identify the phases of the samples before and after the high-temperature oxidation. The elemental mappings were conducted by the electron probe micro-analyzer (EPMA).

Table 3 shows the chemical composition of these alloys by the photoelectric direct reading spectrograph. Figure 1 shows the overall oxidation kinetic curves of the four different samples at 1,300 °C. The type of oxidation kinetics of these samples is parabolic. As it can be observed, the oxidation rate is initially high and gradually lowers with increasing oxidation time. NiCoCrAlY is the current most used bonding coating alloy in the TBC system. The melting point of the NiCoCrAlY alloy is only ~1,400 °C. The oxidation layer of NiCoCrAlY alloys is easily peeled off and disabled quickly at 1,300 °C.

In addition, the $Pt_{82}Al_{12}Cr_6$ and $Pt_{88}Al_{12}$ alloys show a relatively stable stage after exposure for 20 h. Note that in the diffusion-controlled thickening process of alumina (Al_2O_3), the mass gain of the Al_2O_3 scale should follow a parabolic law at the test temperatures according to the classical oxidation theory[32]. The results of oxidation kinetics regarding mass gain with respect to oxidation time can be approximately expressed as[33]:

$$(\Delta m/A)^2 = k_p t \tag{5}$$

where Δm is mass gain of the sample in mg, A is the surface area of the sample in cm², k_p is the parabolic rate constant in mg²/(cm⁴·h), and t is the oxidation time.

Table 3. Measured chemical compositions of the as-prepared alloys

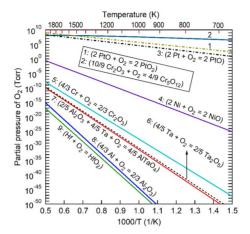| Alloys	Al (at. %)	M (at. %)	Pt (at. %)
$Pt_{88}Al_{12}$	11.78	0	Balance
$Pt_{82}Al_{12}Cr_6$	11.82	6.21	Balance
$Pt_{82}Al_{12}Hf_6$	11.64	6.17	Balance
$Pt_{82}Al_{12}Ta_6$	11.72	6.06	Balance

M: Cr, Hf, and Ta.

Figure 2. Predicted Ellingham diagrams for 9 reactions (see also Table 1) with one mole of oxygen gas (mainly the O_2) and the total pressure fixed at 1 atm. Here, the reaction No. 4 to form NiO is for reference only.

RESULTS AND DISCUSSION

Ellingham diagrams to tailor oxidation resistance

Figure 2 shows the predicted Ellingham diagrams for the nine reactions, as shown in Table 1. The lower the P_{O_2} value [i.e., the lower $\Delta G°$, as shown in equation (3)] indicates that the reaction is more likely to occur. It is seen that Hf is highly susceptible to oxidation (resulting in the formation of HfO_2), even at extremely low oxygen partial pressures (e.g., P_{O_2} = 1.553e-25 Torr at 1,573 K, i.e., 1,300 °C), followed by Al to form Al_2O_3. Besides the Hf- and Al-containing oxides, the oxides $AlTaO_4$, Ta_2O_5, and Cr_2O_3 are also easy to form at relatively low P_{O_2} values. However, the formation of PtO and PtO_2 (and Cr_5O_{12}) is extremely difficult, implying the excellent oxidation resistance of the Pt-based alloys, which is better than the Ni-based alloys, c.f., the formation of NiO in Figure 2. At the present experimental temperature of 1,300 °C, Table 1 also lists the predicted P_{O_2} values, and these reactions are ranked according to the descending order of these P_{O_2} values.

As two examples, Figure 3 shows the formed phases as a function of P_{O_2} at 1,300 °C for two representative alloys, $Pt_{82}Al_{12}Hf_6$ and $Pt_{82}Al_{12}Cr_6$, indicating the dominant fcc phase, together with Al_2O_3 formed for both alloys. In addition, HfO_2 forms for $Pt_{82}Al_{12}Hf_6$ at very low P_{O_2} values and Cr_2O_3 forms for $Pt_{82}Al_{12}Cr_6$ at higher P_{O_2} values (such as > 10^{-7} Torr). In summary, Table 4 shows the oxides predicted for the Pt-rich alloys $Pt_{82}Al_{12}M_6$ (M = Cr, Hf, Pt, and Ta), indicating that Al_2O_3 is easy to form and appears in all $Pt_{82}Al_{12}M_6$ alloys due to the low P_{O_2} value required for the reaction No. 8; c.f., Table 1. In addition, Cr_2O_3 forms for $Pt_{82}Al_{12}Cr_6$, HfO_2 forms for $Pt_{82}Al_{12}Hf_6$, and $AlTaO_4$ and Ta_2O_5 form for $Pt_{82}Al_{12}Ta_6$. Experimental verifications are also listed in Table 4, with details shown in Section "Verifications by oxidation experiments".

Table 4. Summary of the oxides formed in the Pt-rich alloys at 1,300 °C according to the present thermodynamic calculations and the present oxidation experiments

Alloys	Predicted oxides	Measured oxides	XRD figures
$Pt_{88}Al_{12}$	Al_2O_3[a]	Al_2O_3 (α-Al_2O_3 + γ-Al_2O_3)	Figure 4
$Pt_{82}Al_{12}Cr_6$	Al_2O_3, Cr_2O_3[b]	Al_2O_3	Figure 7
$Pt_{82}Al_{12}Hf_6$	Al_2O_3, HfO_2	$(Al, Hf)_2O_3$, Al_2O_3, HfO_2, PtO_2[c]	Figure 10
$Pt_{82}Al_{12}Ta_6$	$AlTaO_4$, Al_2O_3, Ta_2O_5	Al_2O_3, $AlTaO_4$, Ta_2O_5, PtO_2[c]	Figure 13

[a]Al_2O_3 represents the stable α-Al_2O_3 in the present work if there is no further explanation; [b]Cr_2O_3 formed at high P_{O_2} values such as > 10^{-7} Torr; [c]Trace amount or without PtO_2. XRD: X-ray diffraction.
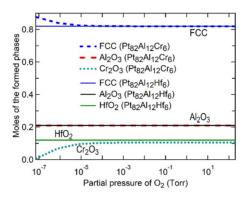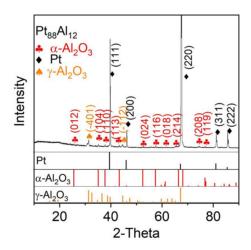

Figure 3. Formed phases for two representative alloys of $Pt_{82}Al_{12}Cr_6$ and $Pt_{82}Al_{12}Hf_6$ at 1,300 °C as a function of the partial pressure of O_2 gas (P_{O_2}), where the input of each alloy is 1 mole and the gas phase is fixed but with zero amount during thermodynamic calculations. Here, we do not distinguish the fcc phase and the $L1_2$ phase, which were modeled by the same sublattice model[20].

Figure 4. Surface XRD results of the alloy $Pt_{88}Al_{12}$ after oxidation at 1,300 °C for 100 h. XRD: X-ray diffraction.

Verifications by oxidation experiments

$Pt_{88}Al_{12}$

Figure 4 shows the patterns of X-ray diffraction (XRD) of the $Pt_{88}Al_{12}$ alloy, which was oxidized at 1,300 °C. Both Al_2O_3 and fcc-based Pt are identified by XRD. Moreover, a few metastable scales of θ-Al_2O_3 are also detected, mainly due to the incomplete phase transition to the stable α-Al_2O_3 during the cooling process of the sample[34]. Note that the present thermodynamic calculations predict only the stable α-Al_2O_3, albeit four kinds of Al_2O_3 (α-, δ-, γ-, and κ-Al_2O_3) are included in the SSUB5 database; see also Table 4.
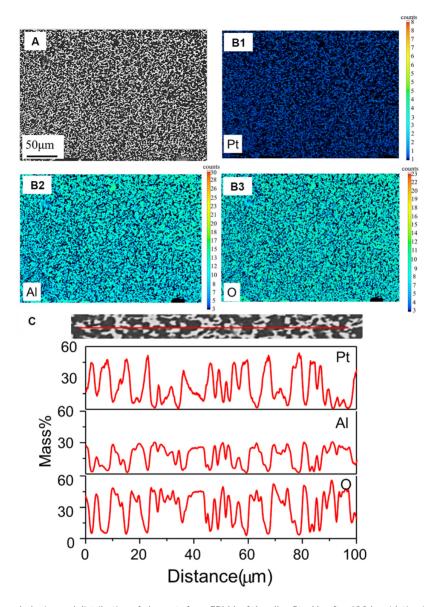
Figure 5. Surface morphologies and distribution of elements from EPMA of the alloy $Pt_{88}Al_{12}$ after 100 h oxidation in air at 1,300 °C. (A) Surface morphology; (B1)-(B3) Pt, Al, and O map distribution, respectively; (C) Linear distribution of Pt, Al, and O.

Figure 5 shows the EPMA elemental maps of $Pt_{88}Al_{12}$ oxidized at 1,300 °C for 100 h. Obviously, the light areas are fcc phase (mainly Pt), and the dark areas are Al_2O_3 according to the EPMA analysis; see Figure 5A. The Al_2O_3 layer is not fully dense. Figure 6 shows the cross-sectional EPMA of $Pt_{88}Al_{12}$ after oxidation at 1,300 °C for 100 h. The oxide scale on the $Pt_{88}Al_{12}$ surface is continuous and intact, which is from 10.1 to 13.3 μm in thickness, as shown in Figure 6A. However, the discontinuous Pt-rich layer is also observed outside the oxide layer, which is probably due to the deposition of the Pt vapor above 1,000 °C[10].

$Pt_{82}Al_{12}Cr_6$

Figure 7 shows the XRD patterns of the $Pt_{82}Al_{12}Cr_6$ alloy after oxidation at 1,300 °C for 100 h. It reveals that the α-Al_2O_3 is the major phase in the oxide layer with small peaks identified as Pt, indicating that Cr promotes the formation of α-Al_2O_3. Different from the case of $Pt_{88}Al_{12}$, after oxidation at 1,300 °C for 100 h, the $Pt_{82}Al_{12}Cr_6$ alloy exhibits a smooth and dense surface. No spallation or crack is observed, and the Al_2O_3
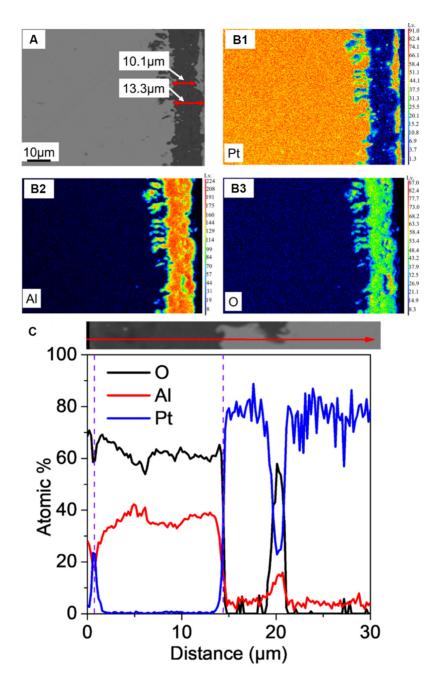
Figure 6. Cross-sectional morphologies and distribution of elements from EPMA EPMA mapping images $Pt_{88}Al_{12}$ after 100 h oxidation in air at 1,300 °C. (A) Cross-sectional morphology; (B1)-(B3) Pt, Al, and O map distribution, respectively; (C) Linear distribution of Pt, Al, and O. EPMA: Electron probe micro-analyzer.

scale adheres well with the base alloy [Figure 8]. Comparing and analyzing the XRD and EPMA results on the surface of the sample after oxidation in Figures 7 and 8, respectively, indicates that a dense Al_2O_3 layer forms on the surface of $Pt_{82}Al_{12}Cr_6$, and the surface of the alloy does not have the element Cr.

Figure 9A shows that the thickness of the Al_2O_3 scale is about 7.3 μm, which is less than the scale of the $Pt_{88}Al_{12}$ alloy. The chemical compositions from the surface to the base alloy $Pt_{82}Al_{12}Cr_6$ are shown in Figure 9B and C. The spikes shown in Figure 9 indicate that Pt is diffused to the interior of the oxidation

Figure 7. Surface XRD results of the alloy Pt$_{82}$Al$_{12}$Cr$_6$ after oxidation at 1,300 °C for 100 h. XRD: X-ray diffraction.

Figure 8. Surface morphologies at EPMA of the alloy Pt$_{82}$Al$_{12}$Cr$_6$ after 100 h oxidation in air at 1,300 °C. (A) Surface morphology; (B1)-(B4) Pt, Al, O, and Cr map distribution, respectively; (C) Linear distribution of Pt, Al, O, and Cr. EPMA: Electron probe micro-analyzer.

layer. Elements Al and O are distributed on the oxidation layer, and the elements Pt and Cr are in the substrate. The concertation of Cr in the substrate is much higher than that in the oxidation layer, suggesting that Cr in Pt$_{82}$Al$_{12}$Cr$_6$ does not participate in the oxidation process. It is hence concluded that no Cr$_2$O$_3$ exists
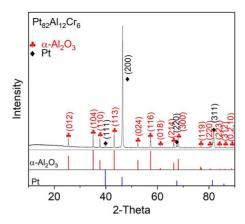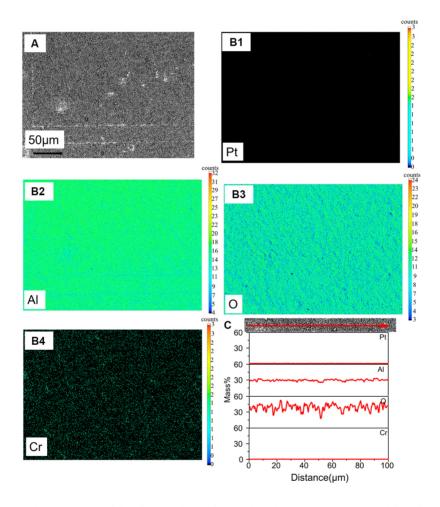
Figure 9. Cross-sectional morphologies and distribution of elements from EPMA EPMA mapping images $Pt_{82}Al_{12}Cr_6$ after 100 h oxidation in air at 1,300 °C. (A) Cross-sectional morphology; (B1)-(B4) Pt, Al, O, and Cr map distribution, respectively; (C) Linear distribution of Pt, Al, O, and Cr. EPMA: Electron probe micro-analyzer.

between Al_2O_3 and the substrate or on the surface of $Pt_{82}Al_{12}Cr_6$. These results are also consistent with the XRD measurements in Figure 7. As seen from the oxidation kinetics of $Pt_{82}Al_{12}Cr_6$ in Figure 1, the oxidation rate is initially high and gradually lowers with increasing oxidation time. During the oxidation process, it forms a continuous and protective Al_2O_3 scale on the surface, and then the oxidation rate reduces, leading to a slower scale growth rate. These results indicate that the dense oxide layer on the sample surface could effectively prevent the external oxygen into the substrate[35] and hence protect the internal stability of the sample[36,37].

Thermodynamic calculations [Figure 3] indicate that Cr_2O_3 will be formed in $Pt_{82}Al_{12}Cr_6$ but at higher P_{O_2} values (e.g., > 10^{-7} Torr), indicating that the P_{O_2} values are not high enough to promote the formation of Cr_2O_3 in the present oxidation process of $Pt_{82}Al_{12}Cr_6$.

$Pt_{82}Al_{12}Hf_6$

Figure 10 shows the XRD results of $Pt_{82}Al_{12}Hf_6$ after oxidation at 1,300 °C for 100 h, confirming the presence of Al_2O_3, HfO_2, and a small amount of Pt on the surface after oxidation. By analyzing the EPMA results, as shown in Figure 11, we observe that the dark area mainly contains the element Hf, which is coincident with the elements O and Al. It is possible that the oxide $(Al, Hf)_2O_3$ has formed due to the solid solution of Hf in Al_2O_3. Therefore, we presume the presence of Al_2O_3 and HfO_2 in the dark region, along with Pt, and possibly
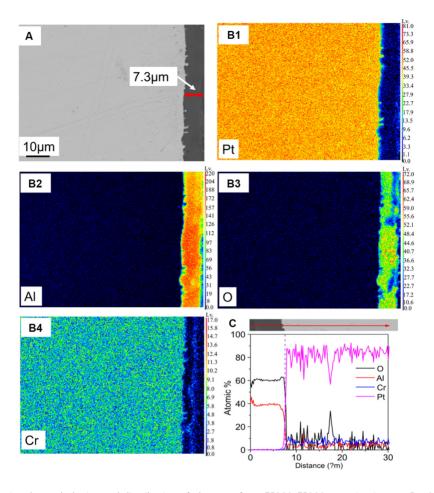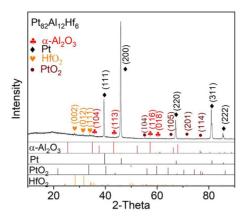
Figure 10. Surface XRD results of the alloy $Pt_{82}Al_{12}Hf_6$ after oxidation at 1,300 °C for 100 h. XRD: X-ray diffraction.

Figure 11. Surface morphologies at EPMA of the alloy $Pt_{82}Al_{12}Hf_6$ after 100 h oxidation in air at 1,300 °C. (A) Surface morphology; (B1)-(B4) Pt, Al, O, and Hf map distribution, respectively; (C) Linear distribution of Pt, Al, O, and Hf. EPMA: Electron probe micro-analyzer.

trace amounts of PtO_2 in the bright region. In addition, it is possible that trace amounts of PtO_2 are present on the surface of $Pt_{82}Al_{12}Hf_6$ after oxidation at very high P_{O_2}. It is worth mentioning that the formation of PtO_2 needs further verification using techniques such as the high-resolution transmission electron microscopy (HRTEM) and/or the electron backscattering diffraction (EBSD).

Figure 12. Cross-sectional morphologies and distribution of elements from EPMA EPMA mapping images $Pt_{82}Al_{12}Hf_6$ after 100 h oxidation in air at 1,300 °C. (A) Cross-sectional morphology; (B1)-(B4) Pt, Al, O, and Hf map distribution, respectively; (C) Linear distribution of Pt, Al, O, and Hf. EPMA: Electron probe micro-analyzer.

Figure 13. Surface XRD results of the alloy $Pt_{82}Al_{12}Ta_6$ after oxidation at 1,300 °C for 100 h. XRD: X-ray diffraction.

Thermodynamic calculations show that only Al_2O_3 and HfO_2 can form [Figure 3] due to insolubility of Hf in Al_2O_3 in the present database and the very high P_{O_2} to form PtO_2; c.f., Figure 2.
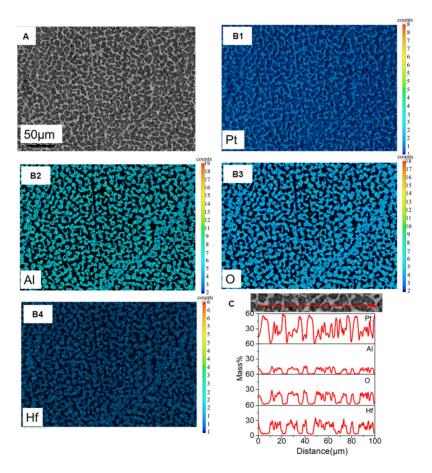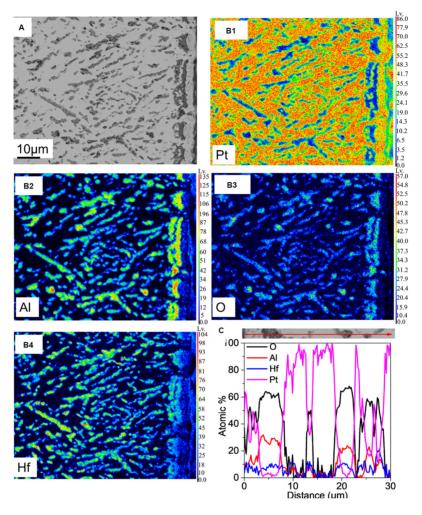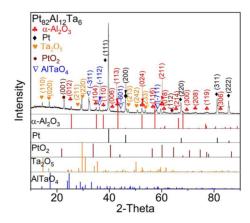
Figure 14. Surface morphologies at EPMA of the alloy $Pt_{82}Al_{12}Ta_6$ after 100 h oxidation in air at 1,300 °C. (A) Surface morphology; (B1)-(B4) Pt, Al, O, and Ta map distribution, respectively; (C) Linear distribution of Pt, Al, O, and Ta. EPMA: Electron probe micro-analyzer.

From the cross-sectional EPMA mapping images of $Pt_{82}Al_{12}Hf_6$, Figure 12A shows that no dense oxide layer is observed, but it forms internal oxides. Figure 12B shows the composition map distribution of these oxides from the surface to the alloy interior. Figure 12B and C reveals that Al and Hf are combined with O. In addition, the dispersive dark appears on the oxide regions with rich Al and O, along with some Hf, observed at a distance of about 4 μm and beyond from the surface. Due to the segregation of alloying elements in oxides, the matrix is almost pure Pt.

In comparison with the $Pt_{88}Al_{12}$ and $Pt_{82}Al_{12}Cr_6$ alloys, $Pt_{82}Al_{12}Hf_6$ shows a worse oxidation resistance due to the extremely easy formation of HfO_2, as indicated by the Ellingham diagrams [Figure 2], resulting in oxidation inside the alloy and the element Pt inside the scale, probably due to a decomposition of PtO_2 at the scale surface after oxidation at 1,300 °C[10].

$Pt_{82}Al_{12}Ta_6$

Figure 13 shows the XRD patterns of $Pt_{82}Al_{12}Ta_6$, which is oxidized at 1,300 °C for 100 h. The oxide layer consists of Al_2O_3, $AlTaO_4$, Ta_2O_5, and PtO_2, agreeing with thermodynamic calculations (except for the formation of a trace amount of PtO_2), c.f., Table 4.
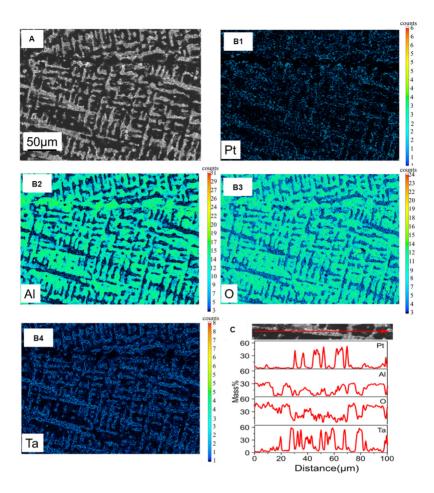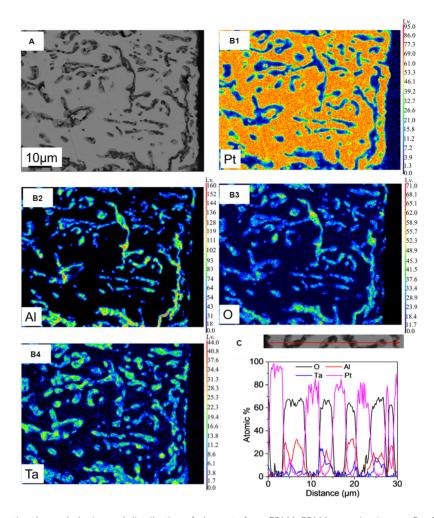
Figure 15. Cross-sectional morphologies and distribution of elements from EPMA EPMA mapping images $Pt_{82}Al_{12}Ta_6$ after 100 h oxidation in air at 1,300 °C. (A) Cross-sectional morphology; (B1)-(B4) Pt, Al, O, and Ta map distribution, respectively; (C) Linear distribution of Pt, Al, O, and Ta. EPMA: Electron probe micro-analyzer.

These results are also consistent with the EPMA mapping analysis [Figure 14], where the dark region is Al_2O_3, and the bright region mainly contains Pt, Ta, and a small amount of O. So, we presume that the bright area mainly consists of Pt, PtO_2, and Ta_2O_5; and Al_2O_3 and $AlTaO_4$ in the dark region; and Ta_2O_5 mainly in the dark area.

Figure 15 shows the cross-section EPMA mapping of the oxidized samples, indicating that no dense oxides on the sample surface are observed. Figure 15B shows that at the interior, both Al and Ta are found in combination with O. According to Figure 15C, the dispersive gray areas are enriched with O and Ta, but almost no Al, which could be identified as Ta_2O_5. The dark oxidized regions with enriched Al and O, along with some Ta, are observed in the interior of the alloy, indicating the formation of Al_2O_3, $AlTaO_4$, and Ta_2O_5. The oxidation kinetics of $Pt_{82}Al_{12}Ta_6$ is similar to that of $Pt_{82}Al_{12}Hf_6$, as shown in Figure 1; even the weight gain is more pronounced, attributed to more intense internal oxides formed than those in the $Pt_{82}Al_{12}Hf_6$ alloy.

CONCLUSIONS

The present work investigates the forming mechanism of oxides in the Pt-based alloys $Pt_{82}Al_{12}M_6$ (M = Cr, Hf, Pt, and Ta) in terms of thermodynamic calculations with experimental verifications. The presently predicted Ellingham diagrams indicate the metals Hf and Al are easy to oxidize, followed by the metals Ta and Cr, while Pt is extremely difficult to oxidize in terms of thermodynamics. Oxidation experiments are characterized by XRD and EPMA, verifying the present thermodynamic predictions and showing that the best alloy with superior oxidation resistance is $Pt_{82}Al_{12}Cr_6$ followed by $Pt_{88}Al_{12}$ by forming the dense and continuous $\alpha\text{-}Al_2O_3$ scale on the surface of alloys after oxidation; while the worse alloy is $Pt_{82}Al_{12}Hf_6$ followed by $Pt_{82}Al_{12}Ta_6$ due to drastic internal oxidation and the formation of deleterious oxides of HfO_2, $AlTaO_4$, and Ta_2O_5.

DECLARATIONS

Authors' contributions

Investigation, Writing - original draft: Chong X

Writing - review & editing: Yu W

Methodology, Visualization, Writing - review and editing: Liang Y

Supervision, Data curation, Methodology, Writing - review and editing: Shang SL

Data curation, Methodology: Li C

Validation, Funding acquisition: Zhang A, Wei Y

Discussion, Funding acquisition: Gao X

Supervision, Methodology: Wang Y

Validation, Supervision: Feng J, Song H

Validation, Funding acquisition: Chen L

Conceptualization, Supervision: Liu ZK

Availability of data and materials

The Supplementary Materials are available including the TDB file for Ellingham Diagrams calculations.

Conflicts of interest

All authors declared that there are no conflicts of interest.

Ethical approval and consent to participate

Not applicable.

Consent for publication

Not applicable.

Copyright

REFERENCES

1. Dinsdale A. SGTE data for pure elements. *Calphad* 1991;15:317-425. DOI
2. Ellingham HJT. Transactions and communications. *J Chem Soc Chem Ind* 1944;63:125-60. DOI
3. Potgieter JH, Maledi NB, Sephton M, Cornish LA. *The platinum development initiative: platinum-based alloys for high temperature and special applications: part IV. platin Met Rev* 2010;54:112-9. DOI

4.   Tesfaye F, Sukhomlinov D, Lindberg D, Taskinen P, Akdogan G. Thermal stabilities and properties of equilibrium phases in the Pt-Te-O system. *J Chem Thermodyn* 2017;106:47-58. DOI

5.   Süss R, Freund D, Völkl R, et al. The creep behaviour of platinum-based γ/γ′ analogues of nickel-based superalloys at 1300 °C. *Mat Sci Eng A* 2002;338:133-41. DOI

6.   Wenderoth M, Völkl R, Yokokawa T, Yamabe-mitarai Y, Harada H. High temperature strength of Pt-base superalloys with different γ′ volume fractions. *Scripta Mater* 2006;54:275-9. DOI

7.   Kim D, Shang S, Li Z, Gleeson B, Liu Z. Effects of Hf, Y, and Zr on alumina scale growth on NiAlCr and NiAlPt alloys. *Oxid Met* 2019;92:303-13. DOI

8.   Wang H, Liu J, Lei S, et al. Effects of Ta and Y additions on the high temperature oxidation mechanisms of Ni-10Al alloy at 1100 °C. *Vacuum* 2023;213:112074. DOI

9.   Yang L, Wang J, Yang R, et al. Oxidation behavior of a nanocrystalline coating with low Ta content at high temperature. *Corros Sci* 2021;180:109182. DOI

10. Odusote J, Cornish L, Chown L. Oxidation kinetics and mechanisms of growth of alumina scale on precipitation-hardened Pt-Al-Cr-Ru alloys. *Corros Sci* 2012;63:119-28. DOI

11. Ross A, Shang S, Fang H, et al. Tailoring critical Al concentration to form external Al_2O_3 scale on Ni-Al alloys by computational approach. *J Am Ceram Soc* 2022;105:7770-7. DOI

12. Golightly FA, Stott FH, Wood GC. The relationship between oxide grain morphology and growth mechanisms for Fe-Cr-Al and Fe-Cr-Al-Y alloys. *J Electrochem Soc* 1979;126:1035. DOI

13. Messaoudi K, Huntz A, Lesage B. Diffusion and growth mechanism of Al_2O_3 scales on ferritic Fe-Cr-Al alloys. *Mat Sci Eng A* 1998;247:248-62. DOI

14. Mora-garcía A, Mosbacher M, Hastreiter J, Völkl R, Glatzel U, Muñoz-saldaña J. Creep behavior of polycrystalline and single crystal Ni-based superalloys coated with Ta-containing NiCoCrAlY by high-velocity oxy-fuel spraying. *Scripta Mater* 2020;178:522-6. DOI

15. Kaplin C, Brochu M. Effects of water vapor on high temperature oxidation of cryomilled NiCoCrAlY coatings in air and low-SO_2 environments. *Surf Coat Technol* 2011;205:4221-7. DOI

16. Backman L, Opila EJ. Thermodynamic assessment of the group IV, V and VI oxides for the design of oxidation resistant multi-principal component materials. *J Eur Ceram Soc* 2019;39:1796-802. DOI

17. Adkison KM, Shang S, Bocklund BJ, Klimm D, Schlom DG, Liu Z. Suitability of binary oxides for molecular-beam epitaxy source materials: a comprehensive thermodynamic analysis. *APL Mater* 2020;8:081110. DOI

18. Shang SL, Lin S, Gao MC, Schlom DG, Liu ZK. Predictions and correlation analyses of Ellingham diagrams in binary oxides. arXiv. [Preprint.] Aug 10, 2023. [Last accessed on 10 Oct 2023] Available from: https://arxiv.org/abs/2308.05837.

19. Thermodynamic properties of inorganic materials . pure substances. Part 1_elements and compounds from AgBr to Ba_3N_2. DOI

20. Kim DE. Thermodynamic modeling and prediction of elastic and thermal expansion properties of Ni-base superalloys: application to Ni-Al-Pt-Cr-Hf system with gamma and gamma' phases. Available from: https://etda.libraries.psu.edu/catalog/12437. [Last accessed on 10 Oct 2023].

21. Kresse G, Furthmüller J. Efficient iterative schemes for ab initio total-energy calculations using a plane-wave basis set. *Phys Rev B* 1996;54:11169-86. DOI PubMed

22. Kresse G, Joubert D. From ultrasoft pseudopotentials to the projector augmented-wave method. *Phys Rev B* 1999;59:1758-75. DOI

23. Perdew JP, Zunger A. Self-interaction correction to density-functional approximations for many-electron systems. *Phys Rev B* 1981;23:5048-79. DOI

24. Perdew JP, Ruzsinszky A, Csonka GI, et al. Erratum: restoring the density-gradient expansion for exchange in solids and surfaces. *Phys Rev Lett* 2008;100:136406. DOI

25. Wang Y, Liao M, Bocklund BJ, et al. DFTTK: Density Functional Theory ToolKit for high-throughput lattice dynamics calculations. *Calphad* 2021;75:102355. DOI

26. Jain A, Ong SP, Hautier G, et al. Commentary: the materials project: a materials genome approach to accelerating materials innovation. *APL Mater* 2013;1:011002. DOI

27. Kirklin S, Saal JE, Meredig B, et al. The Open Quantum Materials Database (OQMD): assessing the accuracy of DFT formation energies. *npj Comput Mater* 2015;1:15010. DOI

28. Perdew JP, Burke K, Ernzerhof M. Generalized gradient approximation made simple. *Phys Rev Lett* 1996;77:3865-8. DOI PubMed

29. Leitner J, Voňka P, Sedmidubský D, Svoboda P. Application of neumann-kopp rule for the estimation of heat capacity of mixed oxides. *Thermochimica Acta* 2010;497:7-13. DOI

30. Kopp H. III. Investigations of the specific heat of solid bodies. *Phil Trans R Soc* 1865;155:71-202. DOI

31. Andersson JO, Helander T, Höglund L, Shi P, Sundman B. Thermo-Calc & DICTRA, computational tools for materials science. *Calphad* 2002;26:273-312. DOI

32. Wagner C. Theoretical analysis of the diffusion processes determining the oxidation rate of alloys. *J Electrochem Soc* 1952;99:369. DOI

33. Lu J, Li L, Chen Y, et al. Y-Hf co-doped AlCoCrFeNi high-entropy alloy coating with superior oxidation and spallation resistance at 1100 °C. *Corros Sci* 2021;182:109267. DOI

34. Wriedt HA. The Al-O (Aluminum-Oxygen) system. *Bulletin of Alloy Phase Diagrams* 1985;6:548-53. DOI

35. Lee D, Santella M. High temperature oxidation of Ni_3Al alloy containing Cr, Zr, Mo, and B. *Mat Sci Eng A* 2004;374:217-23. DOI

36. Levin I, Brandon D. Metastable alumina polymorphs: crystal structures and transition sequences. *J Am Ceram Soc* 1998;81:1995-2012. DOI

37. Zhang Z, Jin H, Mei Ying DL, Chai J, Wang S, Pan J. Origin of anomalous laminar cracking, volume expansion and weight increase of Ti_2AlC MAX phase powders at 600 °C. *Corros Sci* 2020;164:108349. DOI